IEEE Robotics and Automation Letters (RAL) paper presented at the
2020 IEEE/RSJ International Conference on Intelligent Robots and Systems (IROS)
October 25-29, 2020, Las Vegas, NV, USA (Virtual)

Deep Learning Based Real-Time OCT Image Segmentation and Correction for Robotic Needle Insertion Systems

Ikjong Park[1], Hong Kyun Kim[2], Wan Kyun Chung[1], *Fellow, IEEE,* Keehoon Kim[1], *Member, IEEE*

***Abstract*— This paper proposes deep learning based real-time optical coherence tomography (OCT) image segmentation and correction algorithm for vision-based robotic needle insertion systems that can be used in DALK (deep anterior lamellar keratoplasty) surgery. The proposed algorithm provides the position of the needle tip, the lower boundary of the tissue, and the marginal insertion depth solving traditional issues of OCT images like refractive error, optical noise from surgical tools, and the slow speed of volumetric scanning. Through the ex-vivo experiment using 10 porcine corneas, the performance of the proposed algorithm with a robotic system was verified. The segmentation errors were 7.4 μm for the upper boundary, 10.5 μm for the lower boundary, and 3.6 μm for the needle tip. The difference in needle slope between the outside and inside of the cornea was dramatically reduced from 5.87 degree to 0.78 degree. The frame rate of the OCT image was 9.7 Hz, and the time delay of the image processing algorithm was 542.6 ms for 10 images of 512 $\times$ 512 pixels. The results of the proposed algorithm were compared with those of the previous studies.**

I. Introduction

Optical coherence tomography (OCT) allows non-contact observation of cross-sectional tissue images using a safe laser source with long wavelengths (1 μm). OCT has micrometer resolution and millimeter scan range. Therefore, it has been widely used to diagnose corneal and retinal diseases [1], [2].

Recently, the use of OCT has been extended to eye surgeries including corneal transplantation, glaucoma surgery, and retinal surgery [1]. OCT images provide useful information for recognizing the relative position of surgical instruments that can improve the quality of surgical results [3]–[5]. For example, real-time visual feedback from OCT enhanced the accuracy of suturing and needle positioning in corneal surgery and minimized retinal damage during peeling of scar tissue from the retinal surface [6].

In our study, we are particularly interested in OCT image-based robotic surgical systems that allow a needle to be inserted into the cornea for deep anterior lamellar keratoplasty (DALK). In DALK, a 27-gauge needle needs to be be inserted precisely in certain depth, which is neither too deep to penetrate Descemet's membrane or too shallow to fail to separate Descemet's membrane [7]. There have been many previous studies aimed at improving OCT image processing techniques, but there are still unresolved issues in implementing OCT image-based robotic systems, especially in terms of speed and accuracy.

There are trade-offs between scanning range and image processing speed. In [6], though two orthogonal B-scan (tomographic cross-section) images were provided to the surgeon during the insertion of the needle into the cornea, the B-scan plane and the needle plane were frequently

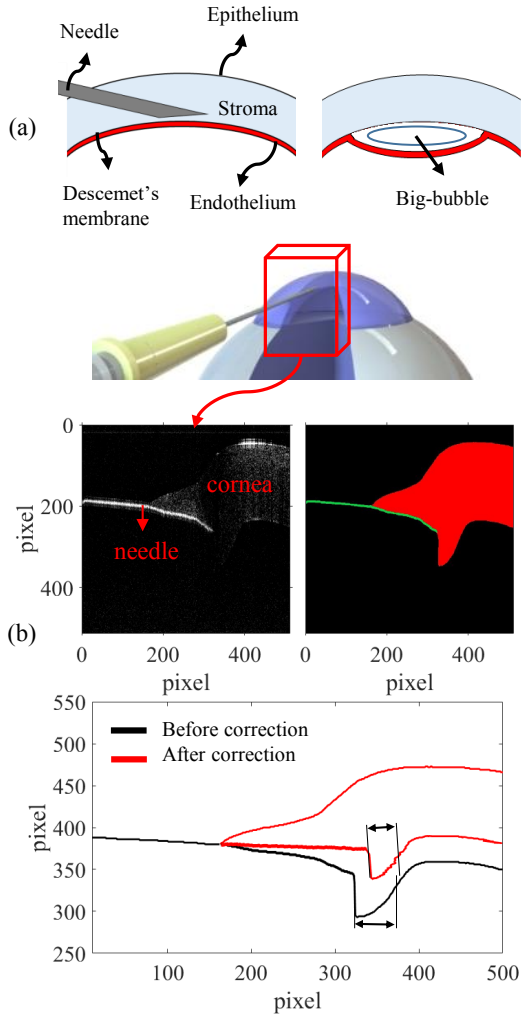

Fig. 1: (a) The structure of the cornea and the procedure of big-bubble technique in DALK. (b) The proposed image processing method.

This paper was recommended for publication by Editor Youngjin Choi upon evaluation of the Associate Editor and Reviewers' comments.This research was supported by the Bio & Medical Technology Development Program of the National Research Foundation (NRF) funded by the Ministry of Science and ICT (NRF-2017M3A9F6029736) and in part by the Industrial Technology Innovation Program (No. 10048358) funded by the Ministry of Trade, Industry & Energy (MI, South Korea).

[1]Ikjong Park, Wan Kyun Chung, and Keehoon Kim are with the Department of Mechanical Engineering, POSTECH, Pohang, 790-784, Korea (e-mail: too1213@postech.ac.kr)

[2]Hong Kyun Kim is with the Department of Ophthalmology, Kyungpook National University Hospital, Daegu, 700-721, Korea

misaligned so that the exact position of the needle tip could not be monitored, and the accuracy of the needle insertion was lowered. Carrasco-Zevallos et al. proposed the real-time 3D visualization of the OCT during surgery [8], but the volumetric frame rate was limited to 1-10 volumes per second to visualize the entire area of the cornea, and a frame rate of 2 volumes per second was chosen to ensure sufficient resolution for the operation. It was not enough speed in a real-time robotic system, therefore, we approaches for real-time recognition of the needle tip and the target tissue.

Another issue is the distortion of OCT images. Due to the curvature of the corneal surface and the difference of refractive index between air and the cornea, the laser ray is refracted at the corneal surface. This phenomenon makes it difficult to visualize the actual shape of the eye and surgical instruments. Ortiz et al. proposed a method of distortion correction, but used normal corneal images that did not include corneal deformity and surgical tools [10]. Distortion correction requires discriminating the background, tissue, and surgical tools in the OCT image. Zhou et al. proposed needle reconstruction and needle tip prediction methods for retinal injection, but the prediction methods had some limitations due to the tissue deformation and absence of distortion correction [9]. Draelos et al. showed that a robotic needle insertion system was more accurate than manual needle insertion [10], [11]. The system used a real-time corneal splitting method, but assumed a paraboloid of the cornea, which cannot be used for incised or severely deformed tissues [12], [13].

The segmentation of medical images using deep learning has been widely studied [14]–[17]. Masood et al. and Dos Santos et al. proposed deep learning based segmentation methods for OCT images and their performance was superior than any other previous methods [16], [17]. The previous studies offered us valuable insight, but those did not provide clear direction to solve the issues, i.e., simultaneous division of both corneal layer and needle in real-time [18]–[20].

In this paper, we propose an image processing algorithm that includes automatic segmentation of OCT images, and distortion correction methods. The image processing methods are integrated with a robotic manipulating system consisting of a three-axis stage and swept-source OCT (SS-OCT).

In order to provide an OCT images closer to the actual geometry, the system uses automatic segmentation using deep neural networks and distortion correction. In addition, the robot manipulation allows to control the OCT scanning range while maintaining sufficient image resolution and eliminating the effects of hand tremor. In the experiment, the accuracy of needle insertion using the proposed system was evaluated using enucleated porcine eyeballs. The insertion procedure during DALK, that requires accurate positioning of a needle between the lower layer of the cornea and the needle tip was performed to verify the performance of the system. Needle control based on the image corrected by the proposed algorithm allowed accurate and safe needle insertion for the big-bubble technique in DALK.

II. The Proposed Method

Fig.2 shows the overall procedure of OCT image processing and the control of the robot based on the result from the image process. In the needle insertion for DALK, the final goal of the proposed algorithm is to control the needle insertion depth (d_s) so that the endothelial layer does not get perforated. To extract information on the needle tip and corneal boundary, semantic segmentation and distortion correction of the OCT image are performed through image processing. v_i is updated by considering the shortest distance (d_s) between the needle tip and endothelial layer of the cornea and image processing delay. When d_s is smaller than the target distance, the insertion is automatically stopped. This section describes the proposed image procession algorithm.

A. Image Segmentation Using Deep Learning

For OCT image-based control systems, the performance depends entirely on image processing speed with sufficient scanning range. The first step of image processing is to extract background, a cornea and a needle from the OCT images in real-time. This subsection describes how to implement a deep neural network for OCT image segmentation.

1) Network Architecture: U-net is well-known segmentation architecture for biomedical images [21]. The network is composed of sequential convolutional blocks that consist of two 3×3 convolutions with the same padding and a rectified linear unit (ReLU), 2×2 max pooling with 2 stride, and 2×2 up convolution with 2 stride (Fig. 3). The U-net structure is modified for our application. A batch normalization layer is added behind every convolutional block for input image normalization and reduction of the training time [22]. The input of the network is a normalized image ($512 \times 512 \times 1$) that is the result of log scaled signal followed by FFT. The output image is $512 \times 512 \times 3$ in size, with each channel representing a different class.

2) Training Data Acquisition and Manual Segmentation: A total of 30 porcine eyeballs were used for the needle insertion experiment to acquire network training images. The porcine eye was placed in a custom-made cornea holder. The range of insertion angle was $\pm 5\,^{\circ}$, and the orientation of needle was downward so that the needle face was toward the posterior surface of cornea. A 27 gauge needle was inserted into the cornea at 0.1 mm/s until it penetrated the endothelial layer. The insertion angle was maintained during the insertion. The needle and cornea were replaced into new ones for each trial. All insertion was performed by using the robotic system (see section III-A). The C-scan range was set to 16.5×1 mm, with 1024×50 sampling points.

Overall, 300 images were chosen from the experiment and were manually labeled into three classes, namely, background, cornea, and needle. Each class can be distinguished by the color: background by black, tissue by red, and needle by green (Fig. 3). Ideally, the needle surface should be represented as a line with single pixel thickness, but the OCT detects the signal reflected from the object and saturation noise appears near the needle because the needle reflects too

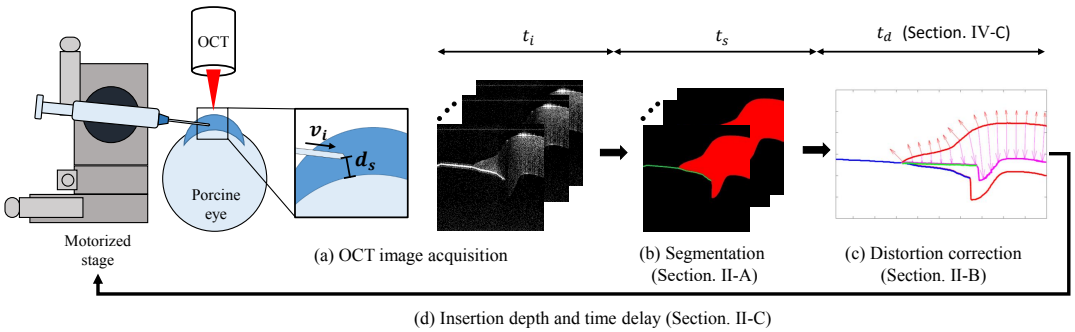

Fig. 2: Overall procedure of needle insertion using the proposed system. (a) Needle insertion conditions are captured by the OCT volume scan. (b) The OCT images are segmented through a deep learning network. (c) The image that contains the longest needle length is selected and image distortion is corrected. (d) By considering needle tip position, lower boundary of cornea, and image processing delay, the insertion speed (v_i) is limited.

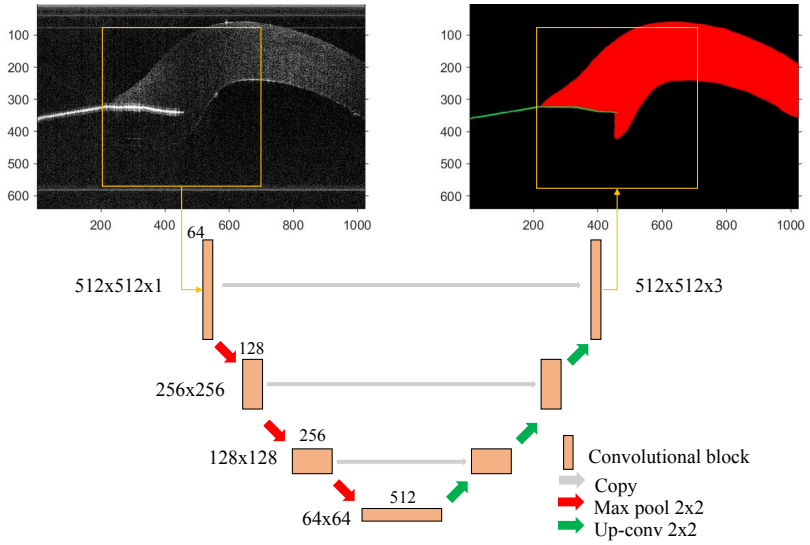

Fig. 3: An example of raw OCT image and corresponding segmentation image. The 512×512 pixel images are used for training U-net. The block size is presented and the size is symmetric with respect to the lowest block.

much light (Fig. 3). For the needle segmentation, three-pixel line was used to represent the straight needle, while expecting that the segmentation method could eliminate the saturation noise.

3) Data Augmentation and Training Environment: Because the amount of training data was limited, the trained network could be overfitted to the given data set. Instead of increasing the number of ground truth images, data augmentation was used to avoid network overfitting. From the raw image of 1024 × 640 pixels in size, three images of 512 × 512 pixels were extracted with random lateral and axial positions (Fig. 3). The scaled raw image was also contained in the training dataset. The intensity of the image was also randomly changed in the range of ±20 % of the maximum intensity. Horizontally flipped images were included to cover the case with different insertion directions.

Overall, 10% of training images were randomly selected as a validation set. Training and validation were executed with an Intel I7-7700 CPU with 3.6GHz, NVIDIA GeForce GTX 1080 Ti with 11GB memory and Keras based on Tensorflow and Python. Adam optimizer with 0.001 learning rate and loss function of binary cross-entropy were used for the training. The training was stopped when the validation accuracy reached 0.99. The total training time was 180 min for the 170 epochs, with a batch size of 5.

B. Refraction Correction of OCT Image

As shown in Fig. 3, the image of the needle inside the cornea is distorted due to refraction. The effect of distortion increases during insertion of the needle due to deformation of the surface. A distorted image can increase the risk of perforation because there is a difference in the needle tip position and the boundary of the endothelial layer represented in the OCT image compared with the actual geometry of the needle and the tissue. Refractive error in the OCT image can

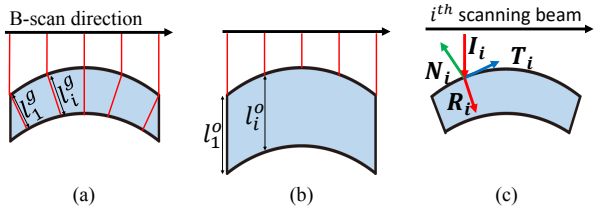

Fig. 4: (a) Schematic explanation of the ray propagation of the OCT and (b) corresponding OCT image. (c) A corrected OCT image and vectors for the correction.

be corrected using vector form of Snell's law [23].

$$\boldsymbol{R_i} = \left(\frac{n_a}{n_t}\right)\boldsymbol{I_i} - \left\{\left(\frac{n_a}{n_t}\right)\boldsymbol{I_i}\boldsymbol{N_i} + \sqrt{1-\left(\frac{n_a}{n_t}\right)^2\left(1-(\boldsymbol{I_i}\boldsymbol{N_i})^2\right)}\right\}\boldsymbol{N_i}, \tag{1}$$

where $\boldsymbol{R_i}$ is the direction vector of the refracted ray, n_a is the refractive index of air, n_t is the refractive index of cornea, $\boldsymbol{I_i}$ is the direction vector of incident ray, $\boldsymbol{N_i}$ is the surface normal vector, and all vectors are unit vectors. Geometrical boundary points can be calculated by multiplying geometrical length with $\boldsymbol{R_i}$.

$$l_i^g = \frac{l_i^o}{n_t}, \tag{2}$$

where l_i^g is the geometrical length of i^{th} ray passed in tissue and l_i^o is the corresponding optical length represented in the OCT image.

Because the B-scan is accomplished by rotational motion of scanning galvo mirrors, it is possible for the OCT image to suffer from fan distortion. $\boldsymbol{I_i}$ can be calculated according to the ray tracing method reported perviously [23]. $\boldsymbol{N_i}$ is calculated from the surface tangent vector ($\boldsymbol{T_i}$), which is calculated from the adjacent surface points. To avoid an abrupt change in direction from the noise of the surface boundary points, moving average filter with a window size of 3 is applied to $\boldsymbol{T_i}$.

C. OCT Scanning Range and Insertion Speed Control

The advantage of robotic needle insertion is that the OCT scanning range can be limited to near the position of the needle tip. Because the needle moves only in the direction in which the needle points, the C-scan range can be reduced. Once the B-scan direction and needle insertion direction coincide, one B-scan image can feature the whole needle including the point of its tip. Fig. 5 shows the B-scan range (l_x) and C-scan range (l_y) when a needle is inserted into the cornea. Because the movement of the needle is limited to the B-scan direction (x-axis), C-scan can obtain an image of the entire needle when l_y is fixed to a value that is larger than the needle thickness. The fixation of l_y results in a decrease of the number of sampling points (n_y) which is directly

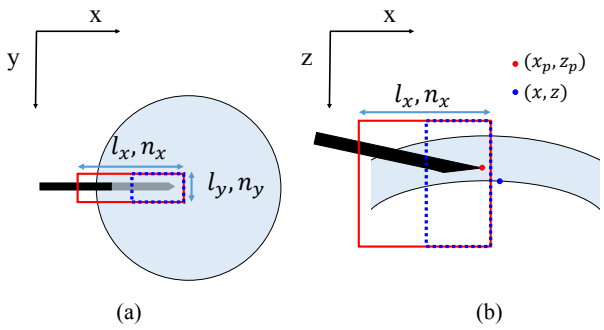

Fig. 5: Schematic explanation of the scanning range and the sampling points from (a) top view and (b) side view. The red box represents initial scanning area and the blue box represents reduced scanning area.

related to the scanning speed. In summary, motorized needle insertion allows an increase in the scanning frame rate.

After finishing the segmentation of n_y B-scan images, one B-scan image that contains the greatest length of needle is selected and distortion correction is applied to that image (Fig.5 (b)). The marginal insertion depth is defined as the shortest distance (d_s) between the needle tip point and the lower boundary of the cornea.

$$\begin{aligned} d_s &= \underset{x>x_p}{\operatorname{argmin}}\, d(x,z) \\ &= \underset{x>x_p}{\operatorname{argmin}} \sqrt{(x-x_p)^2+(z-z_p)^2}, \end{aligned} \tag{3}$$

where x_p and z_p are needle tip points, and x and z are the lower boundary points of the cornea. The lower boundary that is not represented due to optical shadowing ($x \leq x_p$) is excluded. To avoid perforation of the endothelial layer, the insertion speed (v_i) is limited by considering the time delay associated with image processing (t_d).

$$v_i \leq \frac{d_s}{t_d} \tag{4}$$

When the magnitude of d_s is smaller than a certain distance (d_c), a higher resolution image may be required by the surgeon. When using the same number of sampling points along the x-axis (n_x), the B-scan range (l_x) can be reduced so that the accuracy of needle insertion is increased without a corresponding increase in the image processing time (Fig. 5 red and blue box). The detailed application of the proposed method is explained in the experiments section.

D. Image Processing Pipeline

The original processing of OCT image, which does not include segmentation or distortion correction methods, was optimized using parallel computing of CPU threads under the environment of Visual Studio C++ (Microsoft Co.). The signal processing of OCT including background subtraction, spectral shaping, dispersion compensation, zero padding, and FFT was performed using Intel Integrated Performance

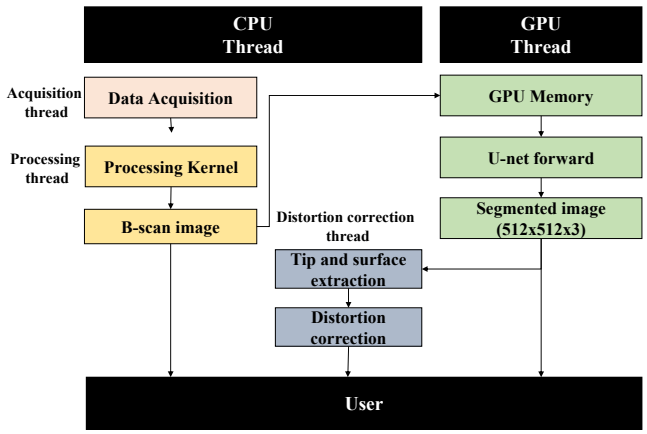

Fig. 6: The raw data acquisition, generation of B-scan image, and distortion correction are performed in CPU threads and segmentation is performed in GPU thread.

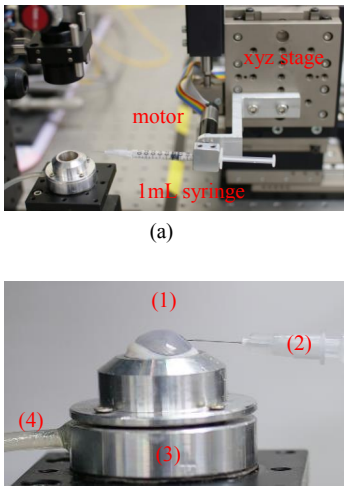

(a)

(b)

Fig. 7: (a) Experimental setting of needle insertion, and (b) (1) porcine cornea, (2) a syringe with 27-gauge needle, (3) a cornea holder, and (4) pressure measuring tube.

Primitives (Intel IPP), which guaranteed the real-time performance of the OCT system without latency (A-scan with 50kHz).

To avoid affecting the speed of real-time signal processing, the segmentation was separated from the signal processing so that it could only be processed on the GPU thread (Fig. 6). The inference of U-net was performed in the GPU under the Python environment with Keras, and for integration with the C++ environment, Boost.Python library was used to implement the Keras library in C++. Following the inference, contour extraction of the needle and tissue boundary and distortion correction were performed in another CPU thread using the OpenCV library. It was confirmed that the added image processing method does not affect the speed of the existing OCT processing via the experiment in the next section.

III. Experimental Setup

An ex-vivo needle insertion experiment using 10 porcine eyes was performed to evaluate the performance of the proposed system regarding needle insertion. Porcine eyes were obtained from a local slaughter-house and the experiment was performed within 6h of enucleation. The cornea extracted from the eyeball was fixed on a cornea chamber (Fig. 7). The intraocular pressure (IOP) of the sample was maintained at 15 mmHg which is within the normal physiological range. A 27-gauge needle and 1 mL syringe were used for the insertion and the needle was changed after every trial.

A. Design of Robot Manipulator

The robot manipulator consists of motorized XYZ linear stages for translational motion, a motor for rotational motion, and a syringe holder that connects the rotational motor and the syringe. Because the cornea ranges from 500 to 700 μm in thickness, the robot manipulator should have motion accuracy in the sub-micrometer range. XYZ motorized stages (LNR50SE, Thorlabs) have a maximum travel range of 50 mm with bidirectional repeatability of 0.5 μm and maximum velocity of 20 mm/s for each axis. A rotational motor (EC-max 16, Maxon) with resolution of 0.002° is used to change the orientation of needle insertion.

The robotic system enables insertion of a needle in a direction consistent with the needle angle. The surgeon can selelct continuous insertion mode, step insertion mode, or angle change mode. While the continuous insertion mode is used at the early stage of needle insertion, step insertion in the sub-micron range is used when the needle is close to the endothelial layer. In the angle change mode, the needle rotates around its end, which means that the tip position remains unchanged.

B. OCT Imaging System

The swept-source OCT (SS-OCT) imaging system with a laser source that has a sweep rate of 50 kHz and a wavelength of 1310 nm (Axsun Technologies) is used to observe the inside of the cornea and the needle position. The frame rate for one B-scan image (2D image) with a size of 500 × 640 pixels is 100 Hz. The maximum field of view of 3D scanning is 16.5 × 16.5 mm, with a penetration depth of 4.5 mm. The axial resolution of the system is 7 μm. The highest lateral resolution is 3.3 μm which can be changed depending on the scanning range and the number of sampling points.

C. Protocol

Before insertion of the needle, the direction of needle insertion was manually aligned with the B-scan direction. The OCT scanning range was initially set to 5.12 × 0.4 mm with sampling points of 512 × 10, namely, $l_x = 5.12\,mm$, $l_y = 0.5\,mm$, $n_x = 512$, and $n_y = 10$ (Fig. 5, red box). In addition to the original OCT images, the corrected

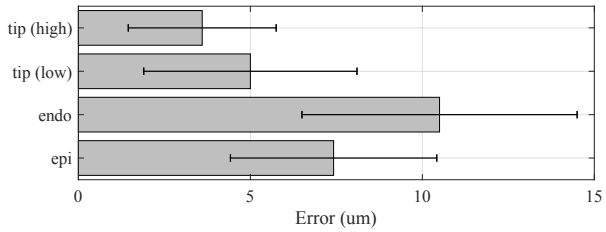

Fig. 8: The results of segmentation error of epithelial layer and endothelial layer in MAE, and tip point error in RMS.

segmentation image, the shortest distance between needle tip and lower boundary, and controlled velocity that had been obtained from the image processing algorithm were provided by the system. The initial insertion speed was set to $500\,\mu m/s$ and the needle insertion was automatically stopped when d_s reached d_t ($50\,\mu m$).

Because our target d_t was 50 μm, the scanning range was reduced by half with the same sampling points when d_s was less than 200 μm, namely, $l_x = 2.56\,mm$ and d_c = 200 μm (Fig. 5, blue box). At the same time, the insertion speed was controlled to $\frac{50}{t_d}\mu m/s$ considering the time delay associated with image processing. After the completion of the needle insertion, air was injected to check whether perforation had occurred.

IV. Results

This section shows the results of the experiments. Section IV-A describes the segmentation accuracy just before the air injection. The distortion correction accuracy using the proposed algorithm is shown in section IV-B. The experimental results after the needle insertion are described sequentially.

A. Segmentation Accuracy

In each trial, one B-scan image obtained just before air injection and four randomly chosen B-scan images were selected to evaluate segmentation accuracy. 50 OCT images were manually labelled by the same method explained in Section II-A.2 and compared with segmentation results from the network.

The mean absolute error (MAE) was used to evaluate the performance of boundary detection of the segmentation method. The MAE of the epithelial layer and endothelial layer was $7.42 \pm 3\,\mu m$ and $10.5 \pm 4\,\mu m$. The error of endothelial layer usually occurred near the needle tip, so the error was larger than that of the epithelial layer. Compared with the epithelial layer, the endothelial layer was more affected by optical shadowing and noise from the needle.

The needle tip point error was defined as the distance between the needle tip position in automatic segmentation images and in manually labeled images. The mean error of the needle tip was $5.0 \pm 3.16\,\mu m$ in low-resolution images and $3.62 \pm 2.16\,\mu m$ in high-resolution ones.

B. Distortion Correction Accuracy

Fig. 9 shows the results of distortion correction. The red line and the magenta line represent the original corneal

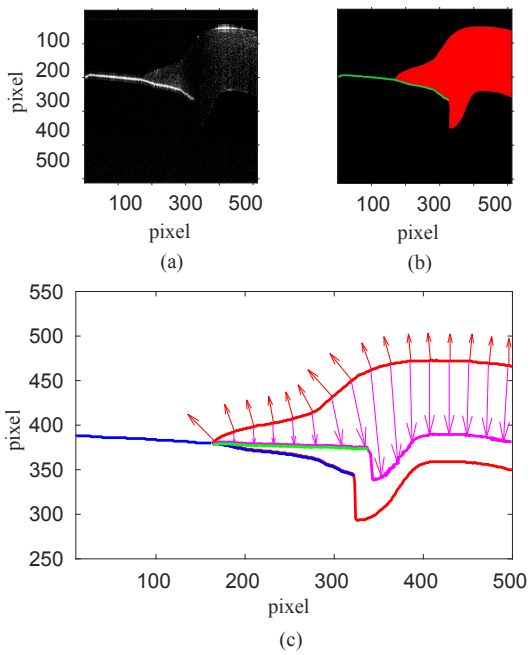

Fig. 9: The distortion correction results (c) of (a) OCT image and (b) segmentation image. Red line: corneal boundary before correction; red arrow: surface normal vector; magenta line: corneal boundary after correction; magenta arrow: the scaled direction vector of the refracted ray; blue line: the needle before correction; green line: the needle after correction.

boundary from the segmentation image and the endothelial boundary after the correction. The green line is the needle inside the cornea, with the data indicating that the entire needle is straightened after the correction.

The accuracy of the distortion correction was confirmed by linear regression of the needle. First, we compared the difference in needle slope between outside and inside the cornea. Second, the entire needle was fitted using linear regression, and then root-mean-square-error (RMSE) was calculated. Table I shows the results of distortion correction. The difference in angle of the needle between outside and inside the cornea reduced $5.87°$ to $0.78°$ and the RMSE of the entire needle was reduced from 14.6 to 0.98 after the correction. This indicates that distortion correction allows images of needle insertion that are closer to the actual state to be obtained[1].

C. Time Delay and Needle insertion results

Since the goal of the needle insertion in DALK is to prevent perforation of the endothelial layer, it is necessary to calculate time delay of the system and the limit of

[1]The needle bending force was measured as 0.062 N, and corresponding needle deflection was calculated using deflection formula of cantilever beam. Considering that the OCT scans the part of the needle in the proposed method, R^2 value was 0.9996 in range of 5.12 mm and 0.9999 in range of 2.56 mm. Therefore, we concluded that the deflection of needle was small enough to be linearly approximated in the OCT scanning range.

TABLE I: Angle and RMSE error before and after distortion correction

	Before Correction		After Correction	
	θ_d(deg)	RMSE (pixel)	θ_d(deg)	RMSE (pixel)
Average	5.87	14.60	0.78	0.98
STD	6.06	3.94	0.62	0.56

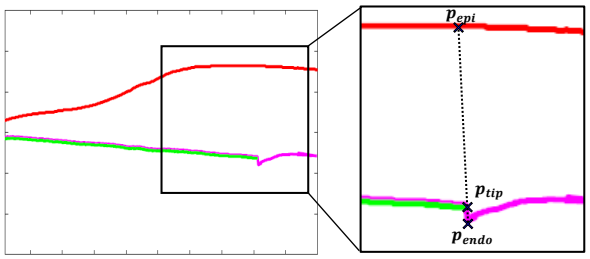

Fig. 10: A graphical representation of the insertion depth ratio. The insertion depth ratio is the ratio between insertion depth (p_{epi} to p_{tip}) and the corneal thickness (p_{epi} to p_{endo}).

needle insertion speed according to the time delay. Image acquisition, segmentation, and distortion correction are the main procedures that can cause the time delay (Fig. 2 (a) - (c)). The image acquisition time (t_i) and segmentation time (t_s) for the 10 B-scan images were 102.4 (9.76 Hz) and $400\,ms$, respectively. The average time for re-scaling and distortion correction was $40.2 \pm 5\,ms$, so the total time delay (t_d) was calculated to be $542.6\,ms$ on average.

From the 10 manually labelled images that were corrected by the method presented in Section II-B, the actual marginal insertion depth and final depth ratio were calculated. The surface normal line that includes the needle tip point was used to calculate the insertion depth and the corneal thickness (Fig. 10). The depth ratio was defined as the ratio between these two values. Table. II shows the depth ratio and marginal insertion depth after the completion of needle insertion. The average insertion depth ratio was 92.45 $\pm$ 2.1% and the marginal insertion depth (d_s) was 55 $\pm$ 1 μm. The error between target d_s and actual d_s was 5 μm. Upon completing the needle insertion, air was injected into the cornea to check for perforation of the endothelial layer. Fig. 11 shows the case when air is injected and we can observe the small air bubbles, which means that the needle did not penetrate the endothelial layer. Perforation of endothelial layer did not occur in any of the cases.

V. Discussion and Conclusion

For the needle insertion in DALK, the proposed system had to control of needle insertion considering the shortest distance (d_s) between the needle and the lower boundary of the cornea. Ideally, safe needle insertion is possible when the needle speed is controlled according to (4) in Section II-C because the needle can be automatically stopped before perforation occurs. In the experiment, the speed was conservatively limited. Instead of updating the insertion speed each time depending on d_s, we assumed a situation of d_s

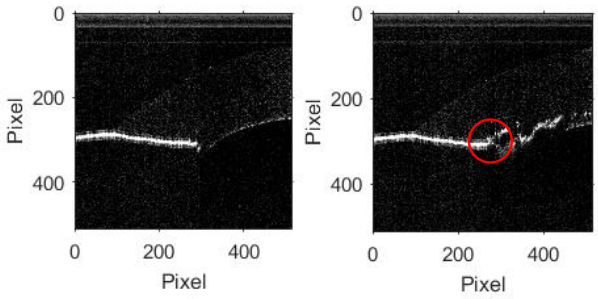

Fig. 11: Air injection after needle positioning. If perforation occurs, air is injected behind the cornea (anterior chamber) and no air bubble is observed. In this case, air is injected into the cornea and the formation of bubbles is initially observed at the needle tip area (red circle).

being the same as the target distance. We believe that such conservative speed control can enhance the safety of needle insertion.

The segmentation accuracy of the proposed method was compared with the segmentation methods proposed in [12], [24], [25] (Table. III)[2]. The segmentation method in [12] supposed the corneal boundary as parabolic shape, which means that this method cannot be applied to other tissues or highly deformed cornea, and the scanning range was fixed to include the apex of cornea in scanning rage. On the other hand, in our method, the scanning range can be reduced while fixing the number of sampling points to increase the resolution of image. Of course, the proposed method requires labelled datasets to training the network. However, by virtue of increase in medical datasets for deep learning, we believe that the proposed methods can be applied for other ophthalmic surgeries, such as retinal injection and corneal suturing.

For the clinical application, the experimental condition has the following limitations. First, although porcine cornea and human cornea have the same layer structure and similar biomechanical properties, the central thickness of the porcine cornea is thicker than the human cornea [26], [27]. As a result, it is easier to insert the needle with a large depth percentage when using porcine cornea. Therefore, we targeted not only the depth ratio in the porcine cases, but also the residual insertion depth of 50 μm. The second limitation is that the movement of an eye was not considered in the experiment. In clinical environment, the patient's eye is not fixed and the eye movement can be generated by the needle insertion force. In that case, the needle tip could be located outside the scanning range, and the proposed method cannot guarantee the accuracy of needle tip position. Active scanning range adjustment and needle pose compensation should be considered in clinical applications.

The proposed method for OCT image processing including segmentation based on deep learning and distortion correc-

[2]Note that the needle segmentation was not performed in [25] and the corneal segmentation was not performed in [24]. The needle accuracy in [24] was calculated by accuracy rate using bounding box

TABLE II: Insertion depth ratio with marginal insertion depth

Trial number	1	2	3	4	5	6	7	8	9	10	Average
Ratio (%)	90.8	91.8	94.0	93.9	91.2	88.0	91.1	95.7	93.6	94.4	92.45
d_s (μm)	50.8	36.9	50.8	50.8	60.3	84.7	49.2	57.2	48.8	61.7	55.1

TABLE III: Comparison of segmentation accuracy

	Epithelial layer (μm)	Endothelial layer (μm)	Needle tip (μm)
Zhou et al. [24]	NA		97.6(%)
Elsawy et al. [25]	5.66 ± 6.38		NA
Keller et al. [12]	24 ± 26	30 ± 32	12
Proposed method	7.42 ± 3.0	10.5 ± 4	3.26 ± 2.16

tion can provide sufficient information to position the needle correctly within the cornea. Through the robotic needle insertion, the scanning range can be decreased while ensuring insertion of the needle to a sufficient depth.

REFERENCES

[1] O. M. Carrasco-Zevallos, C. Viehland, B. Keller, M. Draelos, A. N. Kuo, C. A. Toth, and J. A. Izatt, "Review of intraoperative optical coherence tomography: technology and applications," *Biomedical optics express*, vol. 8, no. 3, pp. 1607–1637, 2017.

[2] M. Pircher and R. J. Zawadzki, "Review of adaptive optics oct (ao-oct): principles and applications for retinal imaging," *Biomedical optics express*, vol. 8, no. 5, pp. 2536–2562, 2017.

[3] V. Scorcia, M. Busin, A. Lucisano, J. Beltz, A. Carta, and G. Scorcia, "Anterior segment optical coherence tomography–guided big-bubble technique," *Ophthalmology*, vol. 120, no. 3, pp. 471–476, 2013.

[4] L. De Benito-Llopis, J. S. Mehta, R. I. Angunawela, M. Ang, and D. T. Tan, "Intraoperative anterior segment optical coherence tomography: a novel assessment tool during deep anterior lamellar keratoplasty," *American journal of ophthalmology*, vol. 157, no. 2, pp. 334–341, 2014.

[5] P. Steven, C. Le Blanc, E. Lankenau, M. Krug, S. Oelckers, L. M. Heindl, U. Gehlsen, G. Huettmann, and C. Cursiefen, "Optimising deep anterior lamellar keratoplasty (dalk) using intraoperative online optical coherence tomography (ioct)," *British Journal of Ophthalmology*, pp. bjophthalmol–2013, 2014.

[6] J. P. Ehlers, J. Goshe, W. J. Dupps, P. K. Kaiser, R. P. Singh, R. Gans, J. Eisengart, and S. K. Srivastava, "Determination of feasibility and utility of microscope-integrated optical coherence tomography during ophthalmic surgery: the discover study rescan results," *JAMA ophthalmology*, vol. 133, no. 10, pp. 1124–1132, 2015.

[7] M. Anwar and K. D. Teichmann, "Big-bubble technique to bare descemets membrane in anterior lamellar keratoplasty," *Journal of Cataract & Refractive Surgery*, vol. 28, no. 3, pp. 398–403, 2002.

[8] O. Carrasco-Zevallos, B. Keller, C. Viehland, L. Shen, G. Waterman, B. Todorich, C. Shieh, P. Hahn, S. Farsiu, A. Kuo *et al.*, "Live volumetric (4d) visualization and guidance of in vivo human ophthalmic surgery with intraoperative optical coherence tomography," *Scientific reports*, vol. 6, p. 31689, 2016.

[9] M. Zhou, K. Huang, A. Eslami, H. Roodaki, D. Zapp, M. Maier, C. P. Lohmann, A. Knoll, and M. A. Nasseri, "Precision needle tip localization using optical coherence tomography images for subretinal injection," in *2018 IEEE International Conference on Robotics and Automation (ICRA)*. IEEE, 2018, pp. 1–8.

[10] M. Draelos, G. Tang, B. Keller, A. Kuo, K. Hauser, and J. A. Izatt, "Optical coherence tomography guided robotic needle insertion for deep anterior lamellar keratoplasty," *IEEE Transactions on Biomedical Engineering*, pp. 1–1, 2019.

[11] M. Draelos, B. Keller, G. Tang, A. N. Kuo, K. Hauser, and J. A. Izatt, "Real-time image-guided cooperative robotic assist device for deep anterior lamellar keratoplasty," in *2018 IEEE International Conference on Robotics and Automation (ICRA)*, 2018.

[12] B. Keller, M. Draelos, G. Tang, S. Farsiu, A. N. Kuo, K. Hauser, and J. A. Izatt, "Real-time corneal segmentation and 3d needle tracking in intrasurgical oct," *Biomedical Optics Express*, vol. 9, no. 6, pp. 2716–2732, 2018.

[13] F. LaRocca, S. J. Chiu, R. P. McNabb, A. N. Kuo, J. A. Izatt, and S. Farsiu, "Robust automatic segmentation of corneal layer boundaries in sdoct images using graph theory and dynamic programming," *Biomedical optics express*, vol. 2, no. 6, pp. 1524–1538, 2011.

[14] A. Mehrtash, M. Ghafoorian, G. Pernelle, A. Ziaei, F. G. Heslinga, K. Tuncali, A. Fedorov, R. Kikinis, C. M. Tempany, W. M. Wells *et al.*, "Automatic needle segmentation and localization in mri with 3-d convolutional neural networks: application to mri-targeted prostate biopsy," *IEEE transactions on medical imaging*, vol. 38, no. 4, pp. 1026–1036, 2018.

[15] P. Zaffino, G. Pernelle, A. Mastmeyer, A. Mehrtash, H. Zhang, R. Kikinis, T. Kapur, and M. F. Spadea, "Fully automatic catheter segmentation in mri with 3d convolutional neural networks: application to mri-guided gynecologic brachytherapy," *Physics in Medicine & Biology*, vol. 64, no. 16, p. 165008, 2019.

[16] S. Masood, R. Fang, P. Li, H. Li, B. Sheng, A. Mathavan, X. Wang, P. Yang, Q. Wu, J. Qin *et al.*, "Automatic choroid layer segmentation from optical coherence tomography images using deep learning," *Scientific reports*, vol. 9, no. 1, pp. 1–18, 2019.

[17] V. A. Dos Santos, L. Schmetterer, H. Stegmann, M. Pfister, A. Messner, G. Schmidinger, G. Garhofer, and R. M. Werkmeister, "Corneanet: fast segmentation of cornea oct scans of healthy and keratoconic eyes using deep learning," *Biomedical optics express*, vol. 10, no. 2, pp. 622–641, 2019.

[18] H. Fu, Y. Xu, S. Lin, D. W. K. Wong, M. Baskaran, M. Mahesh, T. Aung, and J. Liu, "Angle-closure detection in anterior segment oct based on multilevel deep network," *IEEE transactions on cybernetics*, 2019.

[19] K. Nurzynska, "Deep learning as a tool for automatic segmentation of corneal endothelium images," *Symmetry*, vol. 10, no. 3, p. 60, 2018.

[20] T. S. Mathai, K. L. Lathrop, and J. Galeotti, "Learning to segment corneal tissue interfaces in oct images," in *2019 IEEE 16th International Symposium on Biomedical Imaging (ISBI 2019)*. IEEE, 2019, pp. 1432–1436.

[21] O. Ronneberger, P. Fischer, and T. Brox, "U-net: Convolutional networks for biomedical image segmentation," in *International Conference on Medical image computing and computer-assisted intervention*. Springer, 2015, pp. 234–241.

[22] S. Ioffe and C. Szegedy, "Batch normalization: Accelerating deep network training by reducing internal covariate shift," in *International conference on machine learning*, 2015, pp. 448–456.

[23] S. Ortiz, D. Siedlecki, I. Grulkowski, L. Remon, D. Pascual, M. Wojtkowski, and S. Marcos, "Optical distortion correction in optical coherence tomography for quantitative ocular anterior segment by three-dimensional imaging," *Optics express*, vol. 18, no. 3, pp. 2782–2796, 2010.

[24] M. Zhou, H. Roodaki, A. Eslami, G. Chen, K. Huang, M. Maier, C. P. Lohmann, A. Knoll, and M. A. Nasseri, "Needle segmentation in volumetric optical coherence tomography images for ophthalmic microsurgery," *Applied Sciences*, vol. 7, no. 8, p. 748, 2017.

[25] A. Elsawy, M. Abdel-Mottaleb, and M. A. Shousha, "Segmentation of corneal optical coherence tomography images using randomized Hough transform," in *Medical Imaging 2019: Image Processing*, E. D. Angelini and B. A. Landman, Eds., vol. 10949, International Society for Optics and Photonics. SPIE, 2019, pp. 210 – 220. [Online]. Available: https://doi.org/10.1117/12.2512865

[26] A. Elsheikh, D. Alhasso, and P. Rama, "Biomechanical properties of human and porcine corneas," *Experimental eye research*, vol. 86, no. 5, pp. 783–790, 2008.

[27] L. Jay, A. Brocas, K. Singh, J.-C. Kieffer, I. Brunette, and T. Ozaki, "Determination of porcine corneal layers with high spatial resolution by simultaneous second and third harmonic generation microscopy," *Optics express*, vol. 16, no. 21, pp. 16 284–16 293, 2008.